Journal of
Synchrotron Radiation

ISSN 0909-0495

Received 21 June 2005
Accepted 5 January 2006

Recent developments in X-ray imaging with micrometer spatial resolution

Thierry Martin[a]* and Andreas Koch[b]

[a]European Synchrotron Radiation Facility (ESRF), BP 220, 38043 Grenoble, France, and [b]Thales Electron Devices, 460 rue Pommarin, 38430 Moirans, France. E-mail: tmartin@esrf.fr

X-ray detectors for imaging with a spatial resolution in the micrometer and submicrometer range have been developed at synchrotron radiation sources since 1996. The detectors consist of a scintillator, a light microscopy optic and a charge-coupled device (CCD). The scintillator converts part of the X-ray stopped by a material into a visible-light image which is projected onto the CCD by the light optics. A resolution of 0.5 µm FWHM has been achieved using a 1 µm-thick europium-doped $Lu_3Al_5O_{12}$ film. The detective quantum efficiency of the detector is mainly limited by the low absorption of X-rays in the thin layer of the scintillator. To increase the absorption, and therefore reduce the exposure time, new scintillators (Lu_2O_3:Eu^{3+}, Gd_2O_3:Eu^{3+}, Lu_2SiO_5:Ce, $Gd_3Ga_5O_{12}$:Eu^{3+}, $CdWO_4$) have been investigated. These were fabricated using sol–gel and liquid-phase epitaxy processes. Finally, the first fast microtomography experiment including radiation hardness of the optic is shown. This detector uses a high-intensity white beam with 60 keV effective energy and a fast CCD camera at up to 60 frames s^{-1}.

Keywords: X-ray imaging; scintillator; LPE; sol–gel; microtomography; microscopy; CCD.

1. Introduction

Third-generation synchrotron radiation sources offer new possibilities for X-ray imaging with micrometer and submicrometer resolution, owing to the coherence and brilliance of the source. Applications include topography, microtomography and holography.

The two modes of performing microtomography are:

(i) X-ray absorption tomography, which consists of recording the number of transmitted X-rays through the sample. During the path in the sample, the X-rays can interact with matter. Directly transmitted photons project an image of the sample onto the detector. The resulting absorption contrast image is the spatial distribution of the linear attenuation coefficient within the sample, which is placed close to the detector.

(ii) The phase contrast mode requires a coherent beam and an increased distance between the sample and the detector in comparison with the absorption contrast mode. The detector records a spatial intensity distribution owing to interference of the beam across the sample. This method, based on phase contrast, is sensitive to high spatial frequencies. It is two or three orders of magnitude more sensitive than the absorption contrast method and enables weakly absorbing or non-absorbing samples to be imaged effectively. The holotomography mode is an extension of the phase contrast and consists of recording images at different sample-to-detector distances (Cloetens *et al.*, 1999). This mode allows three-dimensional mapping of mass density on the micrometer scale in the material.

The two-dimensional X-ray imaging revolution started with the development of the charge-coupled device (CCD) (Tate *et al.*, 1997). The main advantages of the CCD are that it shows excellent linearity, stability and large dynamic range, it works in real time and the images are read in a few milliseconds after exposure. CCDs used in direct detection are limited in terms of their pixel size (minimum ~6 µm), field of view, sensitivity to radiation damage, and their low X-ray stopping power. Direct detection is mainly used with soft X-rays (Livet *et al.*, 2000). To overcome the stopping power limitation of silicon CCDs, Badel *et al.* (2002) have covered the CCD with a matrix of scintillator columns. An advanced etching technique, inductively coupled plasma, was used to create a matrix of silicon pores which are filled with a CsI(Tl) scintillator of depth 200 µm and pore spacing 45 µm. Although this device fulfils the spatial resolution specification for dental applications, *i.e.* 9 line-pairs per millimeter, the process is not mature for high resolution and defects in the CsI needles are noted.

A solution to improving the X-ray absorption is to couple the CCD to a phosphor. Gruner *et al.* (2002) have given a review of CCD area detectors and show how the CCD has improved the quality for scattering and imaging applications. A typical phosphor screen consists of fine grain powders deposited on a substrate.

doi:10.1107/S0909049506000550

The scintillation light photons suffer multiple scattering as a result of the powdered scintillator grains. This limits the lateral spread of the scintillation light and so degrades the spatial resolution. In addition, the lateral spread increases with increasing phosphor plate thickness, therefore the above-mentioned applications that require high spatial resolution could only be used with thin phosphor screens. Screens based on powder phosphors down to a grain size of approximately 1 µm are commercially available. Their resolution in terms of full width at half-maximum (FWHM) of the line spread function is approximately equal to their thickness. To guarantee a homogeneous screen, at least two to three layers of phosphor grains are necessary and then 2–3 µm resolution can be achieved. To overcome the proportionality between resolution and thickness, 'structured' scintillators have been developed (Nagarkar *et al.*, 1999). This scintillating material is grown in microstructured columns of 5–7 µm diameter, which reduces the width of the point spread function by light guided within columns. This has been achieved with CsI(Tl) columnar growth or by lithographically fabricated phosphor plugs. Detectors configured with this latter technology coupled to a CCD relayed by a 10× microscope objective have produced resolutions of 1 µm at NSLS (Flannery *et al.*, 1987).

An X-ray digital imaging system with spatial resolution of less than 0.5 µm has been demonstrated (Kinoshita *et al.*, 1992; Kimura *et al.*, 1998). This system is based on a 300 nm-thick CsI photocathode evaporated onto a 30 nm-thick gold substrate, an electron lens, microchannel plate, fluorescent screen and CCD. It shows a slightly better spatial resolution than a detector based on a scintillator but it is penalized by remanence of images, a difficulty in approaching the sample owing to the large dimensions ($\sim$1 m length, 0.4 m width by 0.4 m height, $\sim$140 kg) and by a weak X-ray absorption (0.36% at 20 keV).

X-ray imaging with scintillators and microscope objectives has been shown to be a successful approach for obtaining micrometer spatial resolution (Koch *et al.*, 1999). The detectors equipped with a scintillator and CCD camera are close to the spatial resolution limits owing to the indirect detection. The next approach to improving the spatial resolution has two possibilities. The first is to use luminescent screen detectors in the UV wavelength. According to the Rayleigh criteria, $\varepsilon = 0.61\lambda/\mathrm{NA}$, lower wavelengths than visible light could improve the spatial resolution (Chen *et al.*, 2003). In a second approach, Stampanoni, Borchert, Abela & Rüegsegger (2002) have used an X-ray optic based on the principle of asymmetrical Bragg diffraction. The Bragg magnifier system can produce a magnification from 20 × 20 to 100 × 100 and is operated at about 22 keV with a theoretical pixel size from 700 nm × 700 nm to 140 nm × 140 nm. This design, combined with a detector based on a scintillator layer, optic and CCD, has reached submicrometer spatial resolution. The European Synchrotron Radiation Facility (ESRF) has started a nano-imaging program and tested a solution based on the Kirkpatrick–Baez mirror pair (Hignette *et al.*, 2003). The system has produced a spot beam of 86 nm × 83 nm with an output flux of 2×10^{11} photons s^{-1} at 20.5 keV and 80 mA (Cloetens, 2004). Systems based on a Fresnel zone plate, mirror or refractive lenses have recently been developed and have reached 100 nm resolution (Nöhammer *et al.*, 2003; Cloetens, 2004; Lengeler *et al.*, 1999; Schroer *et al.*, 2003).

Systems designed with X-ray optics need a new detector with high detective quantum efficiency (DQE), 0.5 at 20 keV, and the highest spatial resolution possible. Detectors mainly used for tests are based on scintillator crystals or Gd_2O_2S:Tb (P43) type phosphor with lens coupling and a CCD camera; these latter detectors need 50 µm-thick P43 to reach a DQE of 0.5 but a detector will provide a good spatial resolution, roughly 50 µm at FWHM. The gadolinium-oxisulfide-doped terbium can be replaced by a structured scintillator to increase the spatial resolution. The choice of CsI(Tl) is probably not the right solution; radiation damage and light output loss are the source of inhomogeneous response (Hamada *et al.*, 2002; Woody *et al.*, 1992).

Nagarkar *et al.* (2001) have investigated a transparent optical ceramic scintillator for non-destructive testing. Europium-doped lutetium oxide scintillator presents a high density (9.5 g cm^{-3}), high effective Z (63) and is ideal for significant stopping power. In addition, to improve the spatial resolution, the Lu_2O_3:Eu was pixelated. The space between each pixel of 100 µm was filled by dielectric material to guide the light. The real advantages of this device are the improvement of the DQE owing to absorption efficiency, and its emission peak at 610 nm matched well with the CCD camera quantum efficiency. Although the pixel pitch is too large for high spatial resolution, the material is interesting for its performance and has been tested in polycrystalline film form by Garcia-Murillo *et al.* (2002).

Based on the CCD camera, lens combinations and single-crystal film, various high-resolution X-ray detectors have been developed. Micrometer and submicrometer spatial resolution in the 5–100 keV energy range was achieved by combining the microscope objective with the photo-eyepiece in order to magnify the X-ray image onto the CCD camera. The scintillator converts the X-ray image into visible light which is relayed to the CCD.

2. Requirements for scintillators

Thin film scintillators are essential in high-resolution X-ray imaging and show better lateral spatial resolution than powder screens and excellent adhesion to the substrate surface. Different screens allow X-ray imaging; Fig. 1 gives a partial list of phosphors for wide applications in X-ray imaging. To solve the compromise between X-ray stopping power and spatial resolution, single-crystal or polycrystalline film are used.

There are many methods for deposition of luminescent films, including pulsed laser deposition, sputtering, liquid-phase epitaxy and the sol–gel process. The latter technique is suitable for the deposition of amorphous and crystalline thin films through dip- and spin-coating.

Opportunities for improving X-ray detectors in terms of spatial resolution are somewhat limited as they are already near the theoretical limit of 0.4 µm; the best performance

Table 1
Characteristic data of potential scintillators for high-resolution X-ray imaging.

Scintillators	Name	$Z_{\rm eff}$	ρ (g cm^{-3})	$\rho Z_{\rm eff}^4$ ($\times 10^6$)	$\eta_{x/\nu}$	Light yield	λ (nm)	n	Cleavage
Gd_2O_2S:Tb	P43	59.5	7.3	91	13		545		Powder
$Y_3Al_5O_{12}$:Ce	YAG	32	4.55	5	4.0	40000–50000	550	1.82	None
$Bi_4Ge_3O_{12}$	BGO	75	7.13	225		8200	480	2.15	None
$Lu_3Al_5O_{12}$:Ce	LAG	61	6.73	93		20000	535	1.85	None
$Lu_3Al_5O_{12}$:Eu	LAG	61	6.73	93			535	1.85	None
$CdWO_4$		63	7.9	124		15000	470	2.2	Yes
$Gd_3Ga_5O_{12}$:Eu	GGG	52	7.1	80					None
CsI:Tl		54.1	4.52	39	15	65000	540	1.8	None
Lu_2O_3:Eu		68.8	8.4	180		20000	611	1.8	None
Gd_2O_3:Eu		61	7.1	98		19000	611	1.88	None
Lu_2SiO_5:Ce	LSO	65.2	7.4	136		25000	420	1.82	None
$Lu_3Ga_5O_{12}$:Eu	LGG	58.2	7.4	85					None

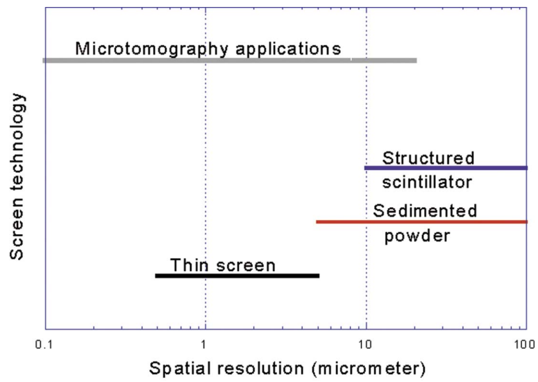

Figure 1
Film requirements for a high-resolution detector based on a CCD.

measured is 0.5 µm FWHM obtained with 1 µm LAG:Eu ($Lu_3Al_5O_{12}$:Eu) thick film and 0.95 numerical aperture (Koch *et al.*, 2000). However, there is also a need for fast X-ray detectors and a short exposure time to reduce the radiation dose to the samples. In the same way, more and more experiment requests are allocated for X-ray imaging and the challenge is to reduce the time required for a microtomography sequence. In this context, improvements could be provided by increased absorption efficiency, increased luminescence efficiency, and emission wavelength optimized for detection by the CCD camera. Commercially available inorganic scintillators, $Y_3Al_5O_{12}$:Ce (YAG:Ce), $CdWO_4$ and $Lu_3Al_5O_{12}$:Eu (LAG:Eu), are used as the sensor material (Stampanoni, Borchert, Wyss *et al.*, 2002; De Carlo *et al.*, 2001; Koch *et al.*, 1998; Beckmann, 2001). However, imaging experiments are performed with high X-ray energies, and scintillators with higher stopping power are necessary; Lu_2SiO_5:Ce (LSO:Ce) was preferred to YAG:Ce by Yagi *et al.* (2004). For various reasons, YAG:Ce and LAG:Eu are less attractive: the light yield of LAG:Eu is low and the undoped YAG substrate of YAG:Ce and LAG:Eu layers emits undesired luminescence (see Fig. 2). This has motivated the X-ray imaging groups of synchrotron radiation sources to search for better scintillators for high-resolution X-ray detectors. Absorption in a scintillator by the photoelectric effect is proportional to ρZ^4 where ρ is the density and Z is the effective atomic number. As a relative measure of efficiency we present these values in Table 1.

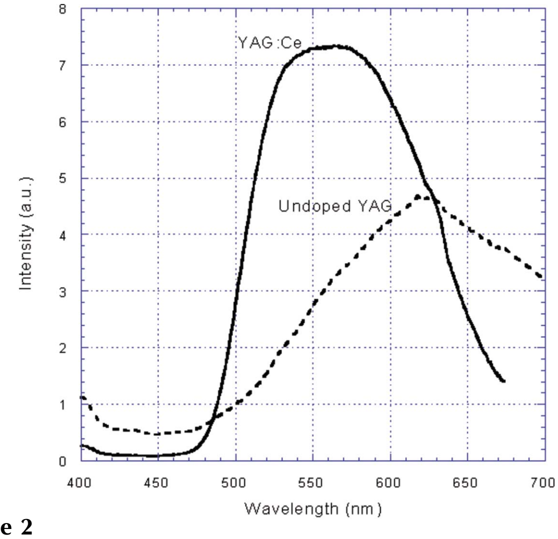

Figure 2
Scintillation spectrum of the emission of 500 µm-thick undoped YAG and 500 µm-thick YAG:Ce single-crystal under X-ray excitation. The data are voluntary cut-offs for long wavelengths, greater than 700 nm, because the sensitivity of the monochromator and photomultiplicator tube limit the accuracy of the data.

2.1. Characteristics of the scintillator

The basic requirements for high-resolution X-ray imaging are:

(i) X-ray absorption: to maximize the X-ray stopping power by the couple, high-density (>5 g cm^{-3}) and large atomic number (>50), and radiation hardness.

(ii) Light emission: high conversion efficiency (>15 visible photons per keV), emission wavelength well matched to the CCD readout (550–650 nm) and low afterglow (2 ms < four decades of magnitude) and linearity of the light with the X-ray flux.

(iii) Optical properties: high transmittance and no scattering.

(iv) Technical aspects: machinable, non-toxic and mechanical strength.

2.2. Physical characteristics

Absorption efficiency for X-rays is maximized by increase of density and effective atomic number. Radiation damage is extremely important in high-resolution X-ray imaging. The first candidate is a bismuth germanate (BGO) scintillator, which shows a high density and a large atomic number. Unfortunately the poor light yield, difficulty in obtaining a smooth surface and its high refractive index are a disadvantage for high-resolution imaging (Tseng *et al.*, 2000). Therefore, BGO seems to be a more attractive scintillator for the high-γ energy counting probes. Cadmium tungstate ($CdWO_4$) is a desirable material for various applications owing to its following properties: high stopping power, high light yield, little afterglow, emission near 470 nm and the fact that it is also non-hygroscopic. However, machining and thinning of a $CdWO_4$ single-crystal is difficult owing to its intrinsic (010) cleavage plane. It is not possible to find commercial $CdWO_4$ scintillators much thinner than 50 µm. Lee *et al.* (1997) have used a 60 µm-thick $CdWO_4$ single-crystal and optics with a numerical aperture of 0.5. The spatial resolution obtained was about 1.5 µm at 20 keV (Koch *et al.*, 2000). Jung *et al.* (2002) have used a $CdWO_4$ single-crystal scintillator cleaved to a thickness of less than 100 µm in a pink beam (non-monochromatic X-ray beam). The spatial resolution was 2.9 µm with an input pixel size of 0.5 µm. To obtain a better spatial resolution, the scintillator must be thinner. A sol–gel processing technique has been applied to produce a thin film of cadmium tungstate (Lennstrom *et al.*, 2003). The resulting film consists of crystal grains of approximately 1 µm in diameter, which is a limitation for high-resolution imaging. An interesting scintillator is the cerium-doped high-density high-*Z* LSO. Although the absorption efficiency of this scintillator is smaller than Lu_2O_3:Eu and BGO, it appears to have a better light yield than BGO and a shorter decay time than Lu_2O_3:Eu. LSO is available from CTI/USA, and Hamamatsu uses this for high-resolution X-ray imaging, and it is currently used at SPring-8. The single-crystal scintillator is 10 µm thick and is glued to an amorphous carbon plate, and Uesugi *et al.* (2001) have achieved 1 µm spatial resolution. The 10 µm thickness is a limitation to the spatial resolution and mechanical polishing cannot reduce this thickness. The next approach is to deposit a single-crystal film or a polycrystalline film on a substrate.

Europium-doped lutetium oxide ($Lu_2O_3:Eu^{3+}$) and gadolinium oxide ($Gd_2O_3:Eu^{3+}$) have been prepared by sol–gel processing. This technique is suitable for the deposition of amorphous and crystalline thin films through dip- or spin-coating. The ESRF and University of Lyons, France, have studied dip-coating for X-ray imaging applications. Multicoating (up to 50 coatings) and heat treatments are required to obtain 800 nm-thick films. The layers are finally annealed for 1 h at 1273 K for high densification and crystallization of the materials. A definite advantage of the sol–gel method as compared with liquid-phase epitaxy is a larger choice of substrate material for crystal growth. Deposition on silicon and silica has been realised by Garcia-Murillo *et al.* (2002). However, this technique is limited in terms of thickness (1 µm) owing to the mechanical stresses between layers. Dujardin *et al.* (2005) have also deposited the same material by a pulse laser deposition process, and they have shown the possibility of depositing a thicker layer by pulse laser deposition, but development is necessary to obtain a homogeneous layer.

The absence of afterglow is an important factor in X-ray imaging. The scintillator afterglow limits the useful dynamic range of the detector at a high frame rate. It is interesting to note that several of the materials have more than one dopant (Eijk, 2003). In general, one dopant is a luminescent ion, while the second is used to reduce the afterglow.

For micrometer resolution, powder phosphor screens like P43 are less suitable because the grain size needs to be very small, *i.e.* around 0.3 µm diameter for 1 µm resolution. Such small grains are not available commercially (Koch *et al.*, 1999). YAG:Ce thin films are commercially available but have low absorption of X-rays in the energy range 5–100 keV. Although the decay of YAG:Ce is an important parameter for fast detectors, the LAG:Eu films have a higher absorption, a lower light output and a net gain of a factor of 4 for a given exposure time above the absorption edge of lutetium (63 keV).

$Gd_3Ga_5O_{12}$ (GGG) scintillators activated by Eu have been grown by liquid-phase epitaxy on GGG substrate. The concentration of Eu was varied to optimize the light yield. Fig. 3 shows the results as a function of europium concentration in atom % of Gd. Layers of different materials have been measured with a CCD camera from PCO, Germany (Sensicam SVGA). The light yield has been measured using an X-ray generator equipped with a Cu anode operated at 20 keV and 40 mA. The emitted radiation has been filtered with a 25 µm-thick copper foil. The light intensity has been recorded with a microscope objective, 4× magnification and a Sensicam CCD. Measurements have been corrected for the absorption efficiency of the scintillator and the quantum efficiency of the CCD. The tested scintillators were a 500 µm-thick mono-crystal of YAG:Ce, 90 µm epitaxy layer of YAG:Ce on an undoped YAG crystal, 50 µm LAG:Eu on undoped YAG, GGG:Eu on pure GGG crystal, LGG:Eu on pure GGG, 800 nm Gd_2O_3:Eu on silica, mono-crystal of $CdWO_4$, 25 µm

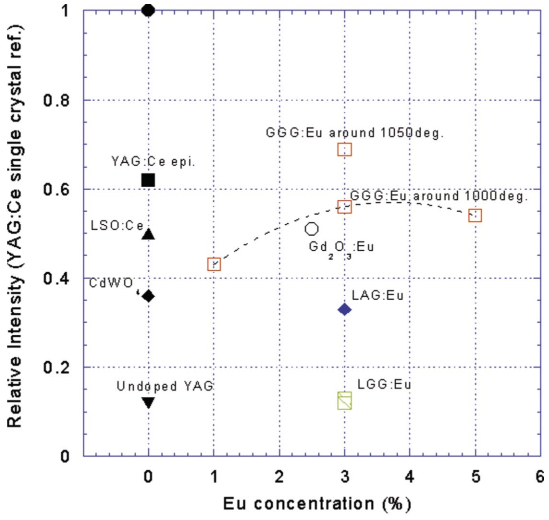

Figure 3
Luminescence efficiency of thin films and single-crystal as a function of the Eu concentration in atom %. The data are referred to the signal response of a YAG:Ce single-crystal (supplier: Crytur).

LSO:Ce on BK7 glass, 10 µm-thick LAG:Ce on BK7 glass, and an undoped YAG single-crystal. The light yield of a monocrystal of YAG:Ce is used as a reference and taken as unity. A concentration of dopant in the melt of about 3% was found to be the value with the highest conversion efficiency for the GGG layer. Compared with LAG:Eu, the absorption efficiency is equivalent and the luminescence efficiency increased. The growth process of LAG on YAG must accommodate their lattice mismatch and this has been achieved with Sc, which substitutes for Al. LAG doped with Eu and Sc has a considerably smaller conversion efficiency compared with GGG:Eu or the epitaxial layer of YAG:Ce. The principal reason for this smaller light yield is the loss of excitation energy on exciting the luminescent centers formed by Sc (Zorenko *et al.*, 2003). The same remarks have been identified by Robertson & van Tol (1984) with In and Pb.

GGG:Eu luminescence results are satisfying because the conversion efficiency is twice that of LAG:Eu. In addition, GGG substrates are free of parasitic scintillation (see Fig. 4). However, indium added in the melt in order to reduce the substrate/film lattice parameter mismatch is assumed to strongly quench light. Further improvements in the efficiency for GGG:Eu might be achieved with a partial substitution of gadolinium by lutetium and bismuth.

Although GGG:Eu, LSO:Ce, Gd_2O_3:Eu and Lu_2O_3:Eu have a similar light yield, the decay time of Ce-doped layers decays more rapidly than for Eu-doped layers; this is preferred for microtomography applications which need an increasingly short exposure time. Therefore the choice of LSO:Ce, YAG:Ce and LAG:Ce seems appropriate with fast microtomography. LAG:Ce is an attractive material. It is now commercially available, non-hygroscopic and, as it is free of cleavage planes, is relatively easy to cut and polish into very thin layers down to 5 µm by a mechanical process (see http://www.crytur.cz/). The first measurement performed by the authors with the 15 µm-thick LAG:Ce is promising: its conversion efficiency, ~48 photons keV^{-1}, is 1.2 times better than YAG:Ce crystal and does not correspond to the published value, 20 photons keV^{-1} (http://www.crytur.cz/). This value needs to be confirmed with LAG:Ce crystals of another sample batch. In addition, the matching with the quantum efficiency curve of the Frelon camera (fast readout low-noise CCD camera at ESRF) with an ATMEL CCD and the Dalsa camera is poor for LSO:Ce but better with LAG:Ce (see Fig. 4). If the LSO:Ce scintillator is chosen, a CCD camera with good short-wavelength quantum efficiency is necessary. On the other hand, LAG:Ce is compatible with all CCD cameras.

Fig. 5 shows the absorption efficiency for a 5 µm-thick layer of YAG, LAG, GGG, LGG, LSO, $CdWO_4$ and Lu_2O_3. A mixture of $Lu_{1.52}Bi_{1.48}Ga_5O_{12}$ deposited by the liquid-phase epitaxy (LPE) process is located between LSO and Lu_2O_3 in terms of absorption. Unfortunately, to reduce the mismatch of the lattice parameters between a GGG substrate and an LGG or an LBiGG film, indium has to be added into the melt. Experimentally, the addition of indium is found to strongly quench the light. LGG:Eu (4 photons keV^{-1}) has been tested and the efficiency relative to GGG:Eu is 24%. Therefore the conversion efficiency of LGG is comparable with pure YAG.

The emission spectrum of thin films is determined by the activator ions added to the host lattice. Both X-ray luminescence spectra and conversion efficiencies have been measured using the same X-ray generator. The light was detected by an Oriel monochromator with 1 nm resolution step and a photomultiplier tube. The detection system was controlled by *Labview* (http://www.ni.com/labview). Fig. 4 shows the quantum efficiency of the Th7899M CCD used in the Pixel Vision and the Frelon 2k × 2k cameras, the THX7887A used in the Dalsa and the ICX285AL in the Sensicam SVGA (PCO). All these CCDs have different quantum efficiencies.

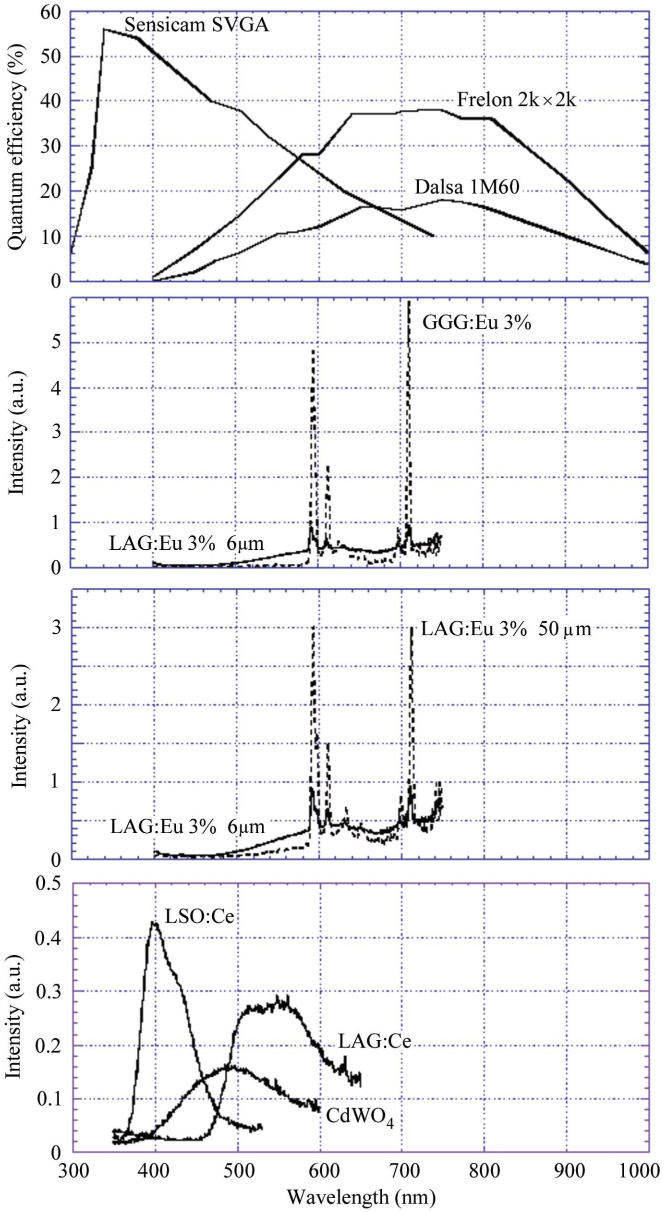

Figure 4
Scintillation emission spectrum of GGG:Eu (3%), 50 µm and 6 µm LAG:Eu (3%), LAG:Ce, $CdWO_4$ and LSO:Ce under 8 keV X-ray excitation. Fast CCD cameras (Frelon 2k × 2k, Dalsa 1M60) have their maximum quantum efficiency at longer wavelengths (750 nm).

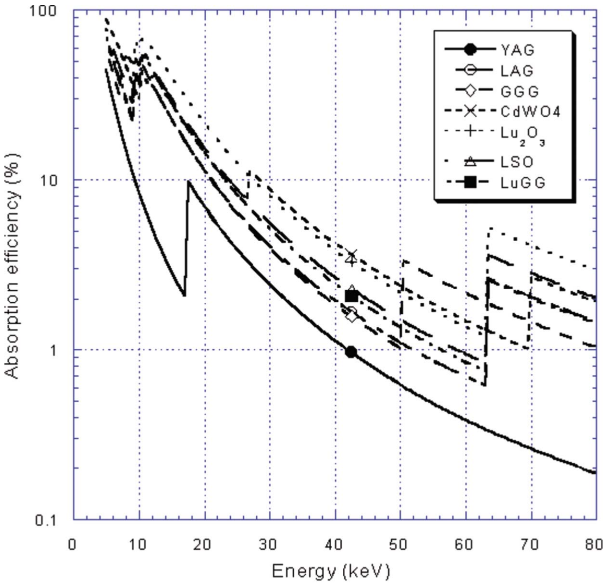

Figure 5
Absorption efficiency of more current scintillators used for high-resolution X-ray imaging for 5 µm-thick layers: $Lu_3Al_5O_{12}$ (6.6 g cm^{-3}), $Gd_3Ga_5O_{12}$ (7.09 g cm^{-3}), $Lu_3Ga_5O_{12}$ (7.5 g cm^{-3}), Lu_2O_3 (8.4 g cm^{-3}), Lu_2SiO_5 (7.4 g cm^{-3}), $Y_3Al_5O_{12}$ (4.55 g cm^{-3}) and $CdWO_4$ (7.9 g cm^{-3}).

Although LSO:Ce and $CdWO_4$ are efficiently detected by the Sensicam, these scintillators are not useful with the Frelon and the Dalsa cameras because ATMEL CCDs show a low quantum efficiency around 450 nm. Europium was chosen for its red emission which is efficiently detected by all three CCD cameras. Undesired luminescence is emitted by the pure undoped YAG and contributes to the signal recorded by the CCD camera. The signal contribution of the YAG substrate can be relatively important for thin layers of scintillators and high-energy X-rays. Fig. 6 shows the ratio between the signal emitted by the scintillator and the signal emitted by the YAG substrate for different layer thicknesses, and it appears that 5 µm LAG:Eu emits the same intensity as 170 µm pure YAG at 20 keV. Therefore, some precautions are required with an undoped YAG substrate at high energies.

3. Spatial resolution

The quality of X-ray images depends on interactions with samples and the detector. Scattering contributes to the forming of the image and degrades the image quality. The most important characteristic of the detector, *i.e.* the spatial resolution, is limited by the X-ray interaction in the scintillator, in the substrate, and by the performance of the optics. There are four kinds of X-ray interactions:

(i) Photoelectric effect and fluorescent radiation. The energy of a photon is completely absorbed by an atom and the photon disappears. An electron is ejected with the energy of the incident photon minus the binding energy of the electron in the atom. After the electron is removed from an internal shell (generally *K* or *L*), an X-ray photon can be emitted. This X-ray photon is emitted isotropically and is called a 'fluorescent X-ray'. The energy can also be transferred to another electron, which is then ejected from the atom. This ejected electron is called an 'Auger electron'. Above the *K*-absorption edge, the primary photoelectric interactions are with the *K*-shell electrons. The resultant *K* X-rays have energies just below the *K* edge. These X-rays may be re-absorbed and deposit energy elsewhere in the scintillator. This results in a loss of spatial resolution in the image.

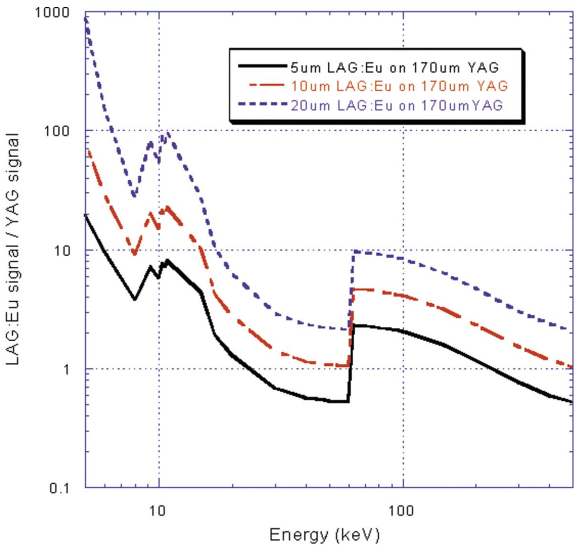

Figure 6
Luminescent contribution of LAG layer and its undoped substrate.

(ii) Rayleigh scattering (or elastic scattering). Photons are deviated from their direction. This is strongly forward-directed and with no loss of energy.

(iii) Compton effect (or inelastic scattering). The incident photon has an inelastic shock with an electron. This electron is free and the photon transfers a part of its energy to the electron. The photon is scattered and the electron obtains kinetic energy.

(iv) Pair creation. This interaction involving the annihilation of the photons appears when incident energy is above 1.02 MeV. Our detectors are not concerned by this interaction.

Therefore the spatial resolution is limited by elastic (Rayleigh) scattering, inelastic (Compton) scattering, which generates fast electrons, and photoelectric absorption, which is a source of fluorescent X-rays. The relative contribution of the three effects *versus* energy, for LAG, YAG and GGG scintillators, is shown in Fig. 7.

The most important interactions of X-rays in matter is the photoelectric effect below 120 keV, 250 keV and 350 keV for YAG, GGG and LAG, respectively. The Rayleigh effect (5%) is the most important scattering effect in the energy range used at the synchrotron radiation sources and is very low compared with the photoelectric effect (95%). The Compton scattering process increases at high energy. For example, the fraction of Compton scattering in the total interaction cross-section increases from 1.2% at 30 keV to 85% at 300 keV for the YAG scintillator. The scattered photon, the energy and direction of which are governed by the Compton scattering distribution, can escape, be scattered again or be absorbed. The resulting electron range, which is very short for low-energy photoelectrons, becomes an appreciable fraction of the scintillator thickness at higher Compton electron energies. The assumption of total electron energy absorption at the interaction site is less accurate. An increasing part of the electron path takes place outside the interaction volume, resulting in the loss of energy absorbed in the phosphor and/or a decrease in the spatial resolution. The average path length travelled by an electron in a YAG crystal is approximately 2.8 µm at 20 keV and 44 µm at 100 keV (http://physics.nist.gov/PhysRefData). This shows that the effect can be an important source of degradation when the Compton effect is dominant. Compton scattering is negligible as a source of background noise in imaging applications for X-ray energy below 100 keV (Hoheisel *et al.*, 2004).

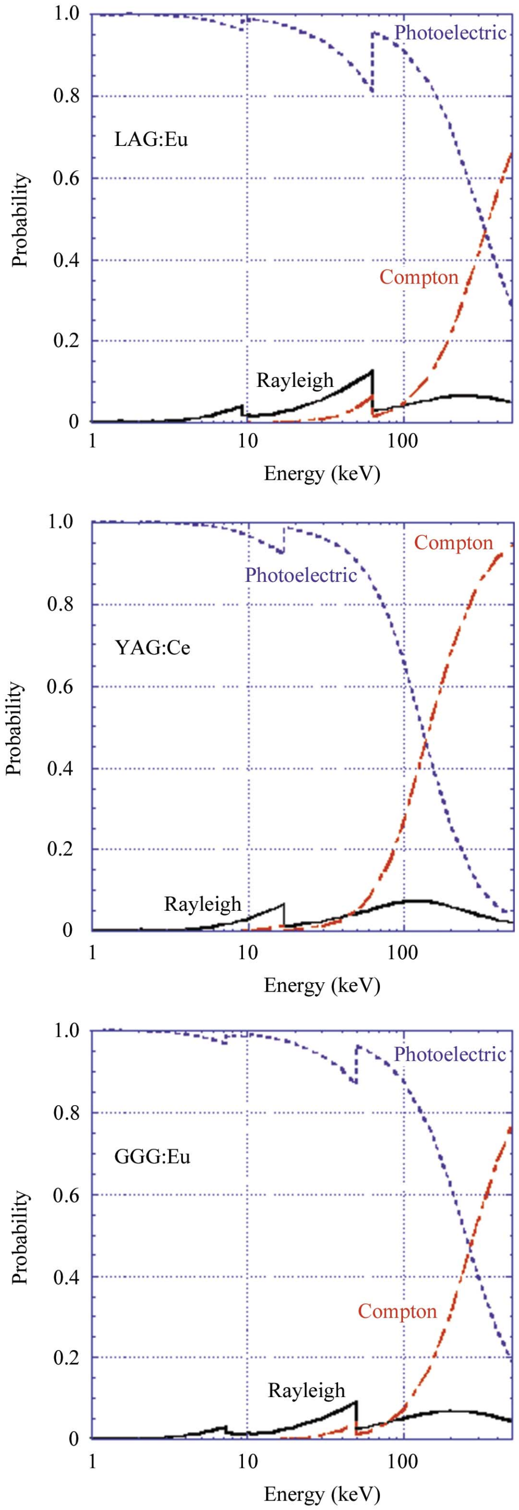

Figure 7
Probability of the three main interactions in LAG:Eu, YAG:Ce and GGG:Eu.

The predominant physical process which reduces the spatial resolution is the fluorescence generated by the photoelectric absorption. Monte Carlo simulations of photon and electron transport have been made for a YAG crystal (Koch *et al.*, 1998). The Integral Tiger Series code uses a Monte Carlo simulation of photon and electron transport in the matter to derive the radial absorbed dose distributions. The calculation used a pencil beam of 14 keV X-rays on a 5 µm-thick YAG:Ce scintillator, itself on a 100 µm-thick undoped YAG substrate. The simulation, which does not take into account the scattering of the emitted visible light, shows a very high absorbed dose in 100 nm FWHM owing to the short path of the Auger electrons. The energy deposited outside the 100 nm is due to secondary electrons and characteristic fluorescence X-rays. On the other hand, calculations at 30 and 100 keV have shown a point spread function tail of the radial energy distribution which degrades the modulation transfer function. The FWHM of the point spread function indicates that the high spatial resolution is thus not limited by the scintillator but by the resolving power of the optics, *i.e.* in particular of the microscope objective.

Another source of tails in the point spread function is the undesired luminescence from the substrate (Ce impurities in undoped YAG). Light emission from substrates has been measured (see Figs. 3 and 4) and corresponds in the worst case to 20% of the luminescence of the YAG:Ce epitaxial layer. This becomes more apparent as thinner layers of scintillator are used (see Fig. 6). Calculation of the ratio of light emitted for three different thicknesses of LAG:Eu layers deposited on 170 µm-thick undoped YAG have been made, with a light yield produced by LAG:Eu equal to 11000 photons MeV^{-1} and 1200 photons MeV^{-1} for undoped YAG (*i.e.* 6% typical value of YAG:Ce). Fig. 4 shows a significant emission of light by the substrate when the LAG layer is thin; the undoped YAG substrate emits more light than the LAG:Eu layer above 20 keV. At high energies, an undoped YAG substrate does not allow the use of very thin LAG:Eu layers. Therefore LAG and YAG scintillators grown by LPE are not optimized for high spatial resolution at high energies. This problem could be solved by using color filters together with LAG:Eu to suppress about half of the substrate luminescence signal. This solution is not adapted to the YAG:Ce layer because the YAG substrate luminescence is close to the YAG:Ce layer emission. Other solutions are to use purer YAG substrates, or some other deposition techniques like the sol–gel method, which permits a larger choice of substrate materials.

Koch *et al.* (1998) have provided a formula to determine the spatial resolution as a function of the optical lens properties. The CCD camera is focused within the scintillator onto the object plane (see Fig. 8). All other planes, in front of and behind the object plane located at z_0 from the surface, are out of the focus but contribute to the total light emitted in the z thickness of the scintillator projected onto the CCD. The image resolution is determined by the defect of focus (δz) of the image distribution outside the object plane. Other degradations of the image are due to the diffraction and the spherical aberrations arising from the thickness of the scintillator (z) and the substrate (t). The parameters affecting the spatial resolution are the following:

Table 2
Some characteristics of different scintillator materials.

The absorption efficiency and DQE are calculated at 20 keV with a 5 μm-thick scintillator layer using expression (1). The resolution is deduced from experiment. Cloetens (1999) have measured a width of the line spread function of 2 μm with NA = 0.3 and 25 μm YAG:Ce. A spatial resolution of 0.8 μm has been measured by Wang *et al.* (2001) with a Nikon Plan Achromat objective with 40× magnification, NA = 0.6 and 5 μm YAG:Ce layer. Stampanoni, Borchert, Wyss *et al.* (2002) have measured a spatial resolution of 1.04 μm with a 1.8 μm-thick YAG:Ce scintillator and 20× NA = 0.7 Olympus optic.

Optic	Material	$\eta_{\text{absorption}}$	DQE (Frelon)	DQE (Dalsa)	Spatial resolution (μm)
10× NA = 0.3	YAG:Ce	0.07	0.021	0.013	2 μm measured (Cloetens, 1999)
	LAG:Eu	0.11	0.031	0.017	
	GGG:Eu	0.11	0.037	0.021	
	Lu_2O_3:Eu	0.21	0.104	0.067	
20× NA = 0.7	YAG:Ce	0.07	0.049	0.038	0.8 μm measured (Wang *et al.*, 2001), 1.04 μm measured (Stampanoni, Borchert, Wyss *et al.*, 2002)
	LAG:Eu	0.11	0.076	0.056	
	GGG:Eu	0.11	0.082	0.063	
	Lu_2O_3:Eu	0.21	0.18	0.15	

$$\begin{aligned}\text{depth of focus} &\simeq \delta z\,\text{NA},\\ \text{diffraction} &\simeq \lambda/\text{NA},\\ \text{spherical aberration} &= t\,\text{NA}^3,\end{aligned}$$

where δz is the depth of focus, λ is the wavelength of light and NA is the numerical aperture.

The spatial resolution is calculated by numerical simulations (Koch *et al.*, 1998) and the resolution can be fitted by

$$R = \left[(p/\text{NA})^2 + (qz\text{NA})^2\right]^{1/2},$$

where p = 0.18 and q = 0.075 (Koch *et al.*, 1998).

The first term is due to the diffraction and the second term to the defect of focus. The spatial resolution is illustrated in Fig. 9 and is expressed as a function of the screen thickness and numerical aperture.

The modulation transfer function (MTF) is used to characterize the spatial resolution of X-ray imaging systems. The MTF is determined by evaluating the response of the system to periodic patterns or by measuring the line spread function using a narrow slit from which the MTF is calculated by Fourier transformation. The MTF can be experimentally obtained in two ways with X-ray generator laboratory equipment or synchrotron radiation source. The first concept uses a tungsten slit. However, the use of a slit requires very precise fabrication and alignment in the beam. The second concept to characterize the imaging system obtains the MTF from the Fourier transform of the measurement of the edge spread function (ESF) by using an absorbing edge. Half of the X-ray beam is absorbed by an object with a straight edge like a 500 μm GaAs crystal, cleaved along its crystal planes perpendicular to its surface. Stampanoni, Borchert, Wyss *et al.* (2002) have measured the ESF with a 100 μm-thick tantalum edge. Contrary to the GaAs edge, which uses a translation movement, they have rotated the edge slightly to oversample the measurement. Some measurement results are given in Table 2. Many groups have a measured spatial resolution of around 1–2 μm. Submicrometer resolution, lower than 1 μm, is more delicate, requiring a scintillator layer thickness of not

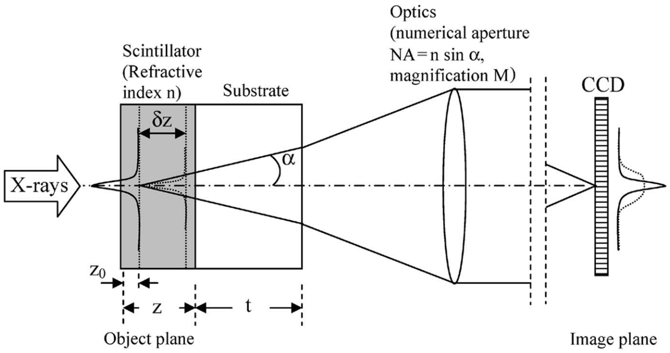

Figure 8
X-ray imaging with scintillators and lens coupling. Identical visible-light images are created by the X-ray beam in different planes of the scintillator. An image in plane z_0 is focused onto the CCD. An image in plane $z_0 + \delta z$ is out of focus at the CCD.

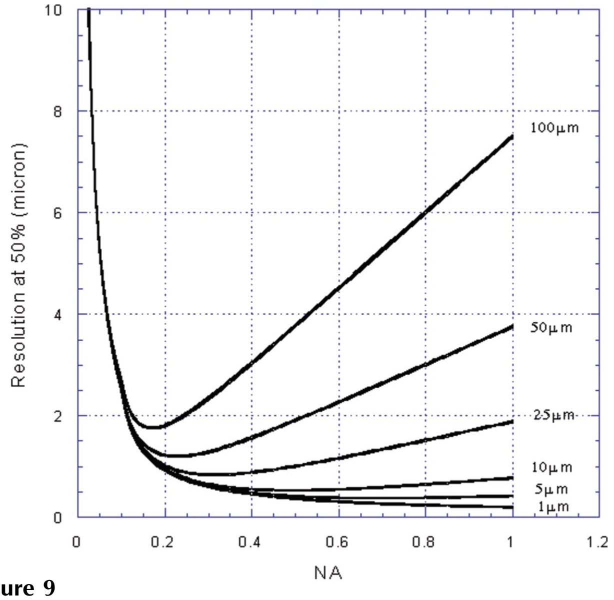

Figure 9
Spatial resolution *versus* numerical aperture NA of an optical system for different thicknesses of the scintillator.

Table 3
Specifications given by the major manufacturers of microscope objectives.

These are compatible with higher-resolution digital camera image data (12-, 14- or 16-bit dynamic range; resolution 1024 × 1024, 2048 × 2048 pixels).

Manufacturer	Tube length (mm)		Parfocal distance (mm)	Magnification/NA	Thread type
	Finite	Infinity			
Ealing	160		34.2–82.2	15×, 0.28 to 74×, 0.65	RMS
Leica		200	45	2.5×, 0.07 to 100×, 0.95	M25
Mitutoyo		200	95	1×, 0.025 to 100×, 0.7	M26 × 0.706
Nikon		200	60	4×, 0.1 to 60×, 0.95	M25
Olympus		180	45	4×, 0.13 to 100×, 0.95	RMS
Spindle	160		45	4×, 0.1 to 63×, 0.85	RMS
Zeiss		165	45	2.5×, 0.06 to 63×, 0.8	RMS

more than 1 µm and high numerical aperture for the objective lens (Koch *et al.*, 2000).

The image properties are qualified by the spatial resolution and by the DQE, which relates the input and the output signal-to-noise ratio,

$$\mathrm{DQE} = \frac{\mathrm{SNR}_{\mathrm{out}}^2}{\mathrm{SNR}_{\mathrm{in}}^2} \simeq \eta_{\mathrm{abs}} \left[1 + \frac{1 + \left(1/\eta_{v/e}\right)}{\eta_{\mathrm{coll}}(E_x/E_v)\eta_{x/v}} \right]^{-1}, \qquad (1)$$

where $\mathrm{SNR}_{\mathrm{in}}$ and $\mathrm{SNR}_{\mathrm{out}}$ are the input and output signal-to-noise ratios of the detector, η_{abs} is the absorption for X-rays in the scintillator, $\eta_{v/e}$ is the quantum efficiency of the CCD, $\eta_{\mathrm{coll}} = (\mathrm{NA}/n)^2/4$ is the collection efficiency of light by an objective with numerical aperture NA in combination with a scintillator with a refractive index n, E_x is the X-ray energy, E_v is the photon energy of the visible-light photons and $\eta_{x/v}$ is the energy conversion efficiency of X-rays to visible-light photons. The DQE, which can never be greater than 1 nor lower than 0, is reduced if the imaging system degrades the spatial resolution, if the detector adds noise to the final image, or does not totally absorb the X-rays. Fig. 10 shows a three-dimensional plot giving DQE expressions as a function of the X-ray energy and numerical aperture for four scintillators: YAG:Ce, LAG:Eu, GGG:Eu and $\mathrm{Lu_2O_3}$:Eu. The *K*-edge of the screen layer, 17.04 keV for YAG:Ce, 50.24 keV for GGG and 63.3 keV for $\mathrm{Lu_2O_3}$, is an important consideration in the detector performance. While it is desirable to use X-rays with energy above the *K*-edge, in order to improve the absorption efficiency the X-ray fluorescence can be re-absorbed by the scintillator layer and a loss of spatial resolution then occurs. The DQE is close to the absorption efficiency in the case of a sufficiently high numerical aperture. High-resolution detectors are mainly used at an energy above the *K*-absorption edge to benefit from the better DQE. As shown in Table 2, the quantum efficiency of the CCD camera and the light yield has an impact on the DQE at low numerical aperture. GGG:Eu and LAG:Eu layers have the same absorption efficiency but we note a DQE improvement for NA = 0.3 of 20% and 23% with the Frelon and Dalsa cameras, respectively. At higher numerical aperture, the improvement is less significant: 8% and 12.5% for the Frelon and Dalsa cameras, respectively. The Frelon and Dalsa cameras are inefficient with LSO:Ce, *i.e.* CCDs are insensitive at 400 nm and thus their DQEs are close to zero. A better solution for fast microtomography is the new fast Dalsa, 1M60P, which uses a FTT1010M CCD and is more sensitive than the 1M60 type, having a DQE of 0.027 with NA = 0.3 and a LAG:Eu layer, which is an improvement of 58%. The choice of CCD camera is more important at low numerical aperture than at a higher one. For example, although the KAF-4320E Kodak, which will be integrated in the third-generation Frelon camera, shows a high quantum efficiency of 70% at 580 nm, *i.e.* 150% more sensitive than the ATMEL CCD, the improvement in the DQE is weak, 0.09 instead of 0.076 with the LAG:Eu layer.

4. Optics coupling

4.1. Refractive objective

High-resolution detectors are based on microscope objectives and adopt two strategies depending on whether they use finite focused or infinity focused optical systems. A finite optical system, or ‘fixed tube length’, is an optical system in which the image is formed by the objective alone; the distance between the microscope objective shoulder and the image seat in the photo-eyepiece is fixed. This distance is named ‘tube length of the microscope’ and is standardized to 160 mm. The situation is different for the infinity-corrected optical systems, where the image is formed by a combination of objective and tube lenses with the microscope objective producing a flux of parallel visible light, imaged at infinity. The tube lens forms an intermediate image in the tube. The magnification produced by an infinity-corrected system is calculated by the ratio of the objective focal length and tube lens focal length.

Table 3 gives a list of the major manufacturers of microscope objectives with their specifications for high-resolution detectors. Finite optical microscopes are less and less commercially available. Spindle sells refractive objectives and Ealing offers reflecting objectives, both with a finite tube length of 160 mm. The situation is different for infinity-corrected optical systems, which are sold by different companies that do not use the same tube lens focal length. Objectives designed for infinity are not usually interchangeable with finite optical tube length and *vice versa* because the infinity lenses suffer from enhanced spherical aberration when used on a finite system. It is possible to use finite objectives with an infinity-corrected microscope but the magnification will be decreased and the spatial resolution degraded. Equally, the mixing of objectives and tube lenses from different manufacturers will result in a change of magnification and a loss of resolution.

For an infinity-corrected optical system, the image distance is set to infinity, and a tube lens is placed between the objective and the photo-eyepiece to produce the intermediate image. Although no degradation has been seen in an inorganic scintillator after several hours in white X-ray beams with inten-

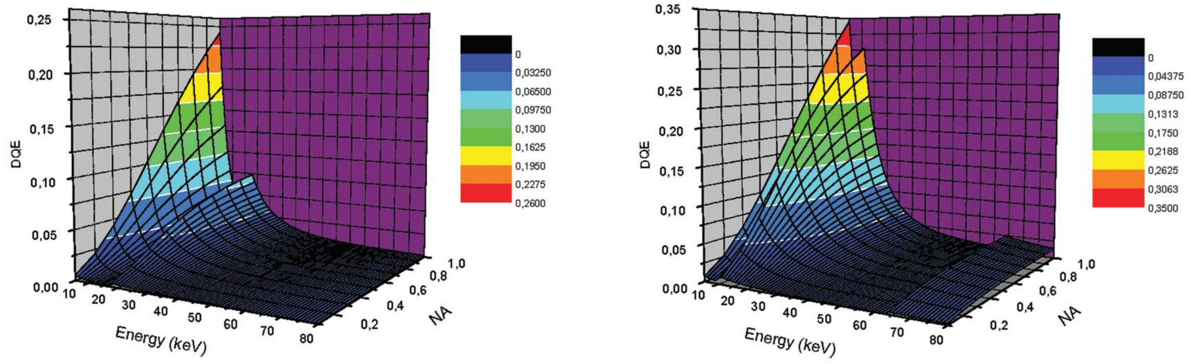

YAG:Ce

LAG:Eu

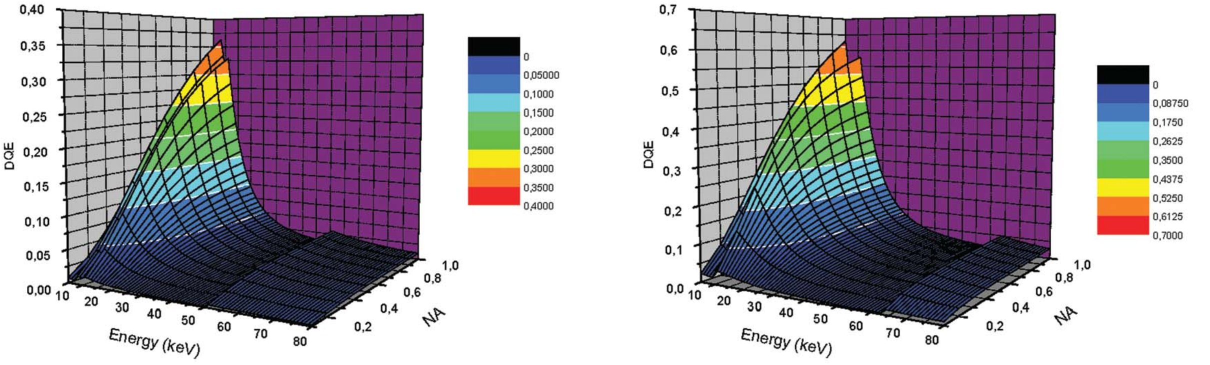

GGG:Eu

Lu_2O_3 :Eu

Figure 10
Three-dimensional mapping of the DQE for an X-ray imaging detector based on lens coupling and 5 µm-thick layer with a Frelon camera.

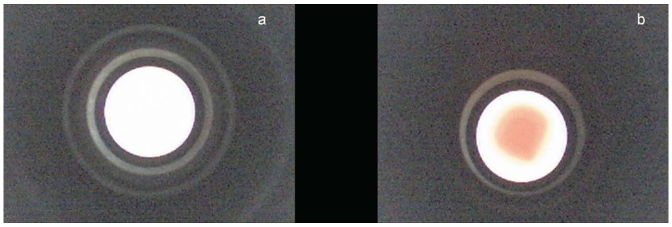

Figure 11
Recorded white illumination relayed by a microscope objective to a CCD camera. (*a*) New microscope objective in white illumination. (*b*) Microscope objective after 70 s in white beam; beam impact is observed by the burnishing of the optic (brown color).

sities of up to 10^{14} photons s^{-1} mm^2 at 65 keV, radiation damage has been observed in the refractive objective after 70 s (see Fig. 11). Some degradation has been observed in the YAG:Ce scintillator using anti-reflection coatings which were deposited to improve the collection efficiency and the resolution. The development of a new detector based on reflected light has been considered to avoid darkening of lenses by the X-rays (Ham *et al.*, 2002). Two methods are possible. The first uses a mirror between the scintillator and the objective. This solution is possible with the infinity-corrected objective; the distance between the objective and the tube lens is variable but the limitation is the working distance of the microscope objective. In practice, a solution can be implemented for magnifications of less than 10×, and for Mitutoyo objectives which use a long working distance, for magnifications from 4× to 100×. The second solution uses a reflecting objective.

4.2. Reflecting objective to prevent radiation damage

Radiation resistance of both the scintillator and the objective lens is necessary. The radiation damage is critical in white beams for refracting objectives. The first method of avoiding this problem uses a plane mirror placed between the scintillator and the microscope objective. The mirror reflects the visible light emitted by the luminescent screen at 90° to the X-ray beam, which prevents radiation damage of the optical components and eases the shielding of the CCD camera. The mirror has to be placed sufficiently far away from the scintillator screen to avoid backscattered X-rays falling onto the screen. This set-up requires a high mechanical precision on the mirror support, which must be fixed at 45° to preserve the parallelism between the shoulder of the objective and the plane object (14 µm depth of focus with 5× magnification, NA = 0.2 objective). An angular misalignment of the mirror is a source of resolution loss as a result of a defocalization. The plane mirror is only conceivable with low magnification. The recent research efforts devoted to decreasing the microtomography acquisition time require the development of a high-resolution detection system for high energy and high intensities (Lame *et al.*, 2003). Typical detector design goals

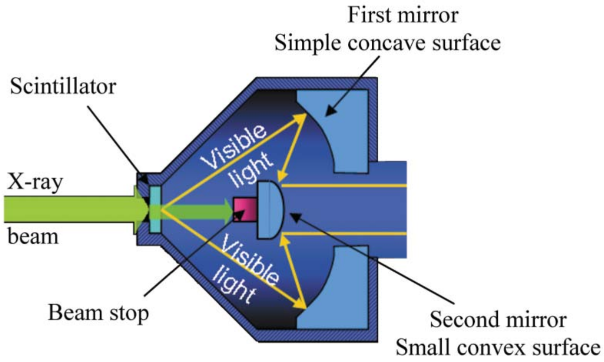

Figure 12
Microscope objective for X-ray imaging system working with pink beam.

include an input pixel size of 1–2 µm, yielding a spatial resolution limit of 4–5 µm with a field of view of 2–3 mm.

Reflecting objectives for microscopes are generally simpler than refractive objectives since they consist only of two mirrors in the Schwarzschild configuration (see Fig. 12). It can be understood as an inverse Cassegrain system, such as in telescopes; the system consists of a concave primary mirror and a convex secondary mirror. Commercial reflecting objectives have a magnification of not lower than 15×. The present application requires a magnification of 5×. Therefore, a specific development was made by Nachet (France) and the ESRF to produce a 5× NA = 0.2 objective. This reflecting objective is shown in Fig. 12: the radius of the primary mirror is 135 mm, the radius of the secondary mirror is 50 mm and the two mirrors are separated by 85 mm. The long working distance of 90 mm has allowed a beam stopper to be fixed in front of the secondary mirror and thus protect the CCD and photo-eyepiece against radiation damage. In this design, the ESRF uses the infinity-corrected system. This solution has allowed us to maintain compatibility with Olympus optics, and intermediate optical components can also be accommodated. No additional optics are needed to correct the image in the 'infinity space' between the objective and the tube lens. Advantages compared with refractive optics are: no scattering from the 45° plane mirror in the folded detector system, and no damage to the optical components owing to protection by the beam stop. The disadvantages are the dimensions (96 mm diameter × 140 mm length), weight and cost.

5. Mechanics

Owing to the high aperture of the microscope objective, the depth of focus is smaller than for a conventional objective; the alignment is therefore much more critical. The focalization using a stepper motor and a gear box gives a precision of 8 steps μm^{-1}. Usually the motor adjusts the scintillator position but for specific design it can also adjust the position of the microscope objective. The use of a motor allows easy focusing, and this can be made automatic by scanning the standard deviation of the image in a region of interest. The ideal focal point is reached with the greatest value of the standard deviation. A misalignment of the scintillator in the object plane occurs in some designs owing to the thickness of the glue used to fix the scintillator on its holder, or errors accumulated in assembling modular system components. To avoid such errors, the adjustment of the scintillator tilt was carried out using a motorized gimbal at the Advanced Photon Source (De Carlo *et al.*, 2001). An additional mirror can be placed behind the microscope objective to deflect the visible light in the perpendicular direction. The goal is to protect the CCD camera against the direct beam (Beckmann, 2001). ESRF detectors are equipped with an additional shielding to further improve the protection of the electronics and the CCD. The mirror is followed by the tube lens, a photo-eyepiece and finally the CCD camera.

The photo-eyepiece relays the image delivered by the objective and projects it onto the CCD plane inside the camera. Photo-eyepieces usually come with low magnification power, from 2× to 5×, because the images are usually projected onto 2/3″ sensors. In our applications, the role of the photo-eyepiece is twofold: firstly to improve the image quality and to correct for vignetting of the field, and secondly to adapt the input pixel size with spatial resolution by increasing the magnification. Although the photo-eyepiece is an advantage with large CCDs, a design based on a 2/3″ CCD does not use a photo-eyepiece as a result of the small dimensions of the CCD.

6. CCD camera

When high spatial resolution is required, the most practical and cost-effective design for relatively fast X-ray imaging is based on CCD detectors coupled to phosphor screen converters by an optical relay. Whereas the spatial resolution and DQE depend on the components used to convey X-ray signals to the CCD, the performance of the fast-imaging system is driven by the readout speed and the dynamic range of the analog-to-digital converter.

With image areas from 1024 × 1024, 2048 × 2048 pixels to 4096 × 4096 pixels in the near future, and 12–14-bit dynamic range, objectives need to record 750 images in 3 s for a single three-dimensional reconstruction, which results in 2 Gbyte of image files. The acquisition of image information of this quantity with a high frame rate (25 frames s^{-1}) initiated the development of detectors for fast microtomography applications. Fig. 13 shows the characteristics of scientific cameras compared with other commercial cameras. There are three suitable categories of system on the market. The first is the slow-scan camera which approaches 16 true bit depth with long exposure times as a result of the cooling system (Wang *et al.*, 2001). Secondly, a large choice of 12-bit CCD cameras with different pixel resolutions are sold for versatile applications in terms of a compromise between frame rate, bit depth and dark current (Jung *et al.*, 2002). In this category, fast cameras offer 30–60 frames s^{-1} and are used only for fast tomography. The third category is the most popular for tomography applications: the Kodak KAF-1602E from Apogee with 1024 × 1536 pixels, 9 µm × 9 µm pixel size, 1.3 MHz (Ham *et al.*, 2002; Beckmann, 2001), and the ATMEL TH7899M with 2048 ×

2048 pixels, 14 µm × 14 µm pixel size, 20 MHz from Pixel Vision (Stampanoni, Borchert, Wyss *et al.*, 2002), Frelon 2k (Bravin *et al.*, 2003) and Frelon2014 are four examples and are used for the compromise between frame rate and dynamic range.

In detectors based on CCDs, noise can be categorized as internal: the overall noise associated with the acquisition of an image is the readout noise, the dark-current noise and the photon shot noise associated with the signal. Noise categorized as external includes radiated electromagnetic interference and 50 Hz noise from the power supply.

The readout noise depends on the readout speed (usually the faster the readout rate, the higher the noise) and the electronics controlling the CCD. Thermal energy creates electrons in the pixel well, *i.e.* dark current. The dark current is highly temperature-dependent, hence the CCDs are cooled by thermo-electrical cooling (Peltier elements) with forced air, water or liquid nitrogen cooling to reduce the dark current, thus allowing long exposure times. The photon shot noise is a fundamental property of the quantum nature of light. According to statistical theory the number of visible photons collected by the CCD will exhibit a Poisson distribution. The charge induced by photon shot noise will also be Poisson distributed. The magnitude of the noise equals the square root of the number of corresponding signal photons.

Table 4
Measured characteristics of CCD cameras used at the ESRF for tomography.

	Sensicam	Frelon 2k First generation	Dalsa 1M60	Frelon 2k14 Second generation
CCD chip	ICX285AL	TH7899M	THX7887A	TH7899M
Number of pixels	1376 × 1040	2048 × 2048	1024 × 1024	2048 × 2048
Bit depth (bits)	12	14	12	14
Pixel size (µm × µm)	6.45 × 6.45	14 × 14	14 × 14	14 × 14
Nyquist resolution (line-pairs mm^{-1})	77.5	35.7	35.7	35.7
Speed (MHz)	16	4 × 5: 20	4 × 20: 80	4 × 10: 40
Frame rate (frames s^{-1})	8	4.2	60	8.2,† 15.3‡
Sensitivity (e^{-}/ADU)	4	20	50	20
Readout noise (e^{-})	5	20	48	23
Full-well capacity (e^{-})	18000	320000	205000	320000
Dark current (e^{-} s^{-1} pixel^{-1})	<0.1	3 (253 K)	452 (298 K)	1 (253 K)
Integral non-linearity	–	±0.3%	±0.6%	±0.6%

† In full frame mode, where an exposure is taken, the shutter closed, and the CCD readout during a given time. ‡ In frame transfer mode, where the CCD contains a storage zone to which the image is very quickly transferred (typically < 5 ms). The next exposure can be started while the storage area is read out.

The Frelon camera was developed at the ESRF for fast imaging experiments, based on an ATMEL CCD of 2048 × 2048 pixels, which offers four outputs. The Frelon camera is cooled to 253 K to reduce the dark current for long exposure times. It uses a full-frame transfer CCD, which allows groups of several pixels to be binned within rows or columns, definition of the region of interest for selected read out, and the following three readout modes:

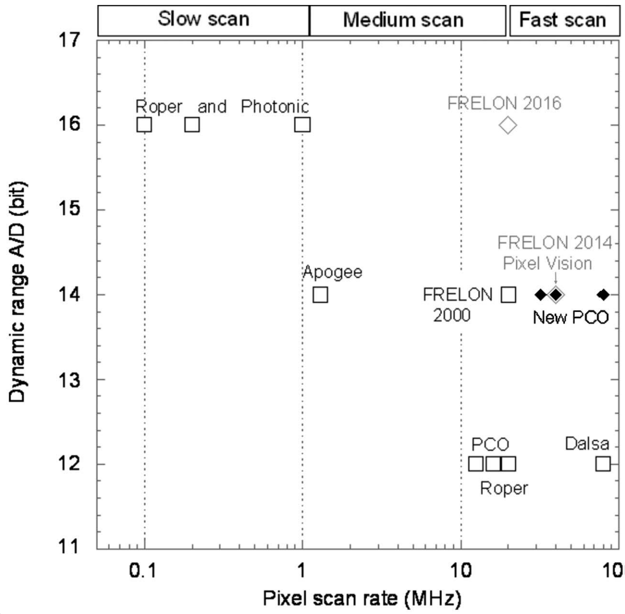

Figure 13
Present situation (squares) of cameras used on high-resolution detectors and future situation (diamonds) of the scientific cameras for high-resolution detectors in terms of the dynamic range of the A/D converter.

(i) Standard full-frame mode, which allows 4.2 frames s^{-1} to be recorded in the limit of zero exposure time.

(ii) A kinetic 'pipeline mode' readout has been implemented for fast tomography. One or more exposed lines are shifted to the two nearest outputs and are read out in synchronization with the sample movement. The user creates a physical area near the top or bottom of the CCD that will be under exposure while the rest of the CCD is masked. The constraints applied to the exposed area are the following: the value must be equal to 2^n where $n = 0 \ldots 11$. In order to accelerate the image acquisition frequency, the size of the exposed area should be as small as possible because of the time required for the signal readout. The CCD is read with one or two outputs of a single readout register. In the kinetic pipeline mode, when the integration is finished, the image is read out and a new integration can then restart. A minimum dead time of 850 µs between the acquisitions of two lines is necessary in order to allow the line shift and the readout. 256 lines × 2048 columns can be recorded in 58 ms, *i.e.* 17.3 frames s^{-1}.

(iii) A new generation of Frelon camera, called 2k14, is under development. The new system will allow the present readout speed (4 × 10 MHz) to be increased and a frame transfer mode (use of a memory zone) to be added. The frame transfer mode may result in a frame rate increase of up to a factor of two with almost no lost time between acquisition of successive images. The first results are given in Table 4. The readout noise is ∼20 electrons for both the old and new Frelon, corresponding to 1 ADU.

The first fast microtomography experiment was completed in 30 s with a 1k × 1k Frelon, for a total of 500 projections at different angles with 60 ms frame time each (20 ms for exposure time, 35 ms for readout time and 5 ms for opening and closing the X-ray shutter). The PC was a Linux PIII 500 MHz with 256 MB of RAM memory to allow the image to be stored in memory while acquiring data. To be able to save onto a disk, this PC was equipped with four fast disks. A tomography data set of 500 images of size 128 × 512 pixels requires a total of 64 MB memory, but for saving bigger images the RAM memory of the Linux PC needs to be increased. Higher frame rate is necessary for fast tomography using white beams. A high-speed imaging system dedicated to fast tomography was developed by integrating a high-speed CCD camera (Dalsa 1M60) with a custom acquisition system. Here, the 12-bit camera uses a 1k × 2k CCD operating in frame transfer mode with a 1k × 1k active area acquiring full images at up to 60 frames s^{-1}. This CCD camera is convenient on several points: in addition to its fast imaging, the 1M60 is an inexpensive camera, commercially available, lightweight and conveniently assembled with optics; on the other hand this CCD camera is not cooled and therefore does not allow long exposure times. Table 4 summarizes the measured characteristics of the main cameras used for microtomography at the ESRF.

7. Applications

An X-ray microtomography detector associated with synchrotron radiation is a non-destructive powerful instrument for studying the internal properties of a sample under conditions of temperature or pressure. It enables *in situ* visualization of damage or evolution in materials science, medicine and biology.

The brilliance of the synchrotron radiation beam, together with the recent improvements in data collection *via* a PCI 64-bit bus and storage devices have allowed the three-dimensional microstructural evolution of materials to be recorded during sintering on the micrometric scale. Two materials have been investigated on the ID15 beamline of the ESRF: a loose copper powder and a steel powder compact (Lame *et al.*, 2003). The pink X-ray beam is produced by a wiggler and filtered by Cu to remove low-energy photons. A furnace is located between the fast X-ray shutter placed upstream of the sample and the X-ray detector. The sample is mounted on a translation and rotation table to displace and rotate it in the beam during the tomography. The detector is based on a Frelon CCD camera for speed and resolution, a 6 µm-thick LAG:Eu scintillator and a 15× reflecting microscope optic, NA = 0.5. The conventional data acquisition for tomography is a sequential structure where operations are the following: shutter opening, CCD exposure, shutter closing, CCD readout, data storage on hard disk, sample rotation, shutter opening *etc.* Typical acquisition time is about 10–15 min for 1000 radiographs. As part of the ID15 'fast-microtomography' development, *i.e.* a 1 min time-scale acquisition, the data acquisition is modified; the sample has a continuous rotation during which the following procedure is carried out: shutter opening, CCD exposure, shutter closing, CCD readout to RAM, shutter opening *etc.* (see Fig. 14).

The thermal cycle of the copper powder and three tomographic projections are shown in Fig. 15. An evolution is clearly seen during the thermal cycle. The first projection is the start of bonding between particles which are mainly dispersed. In the second projection, neck growth is clearly observed between particles and the porosity is reduced. After sintering above 1323 K, the third projection shows the final evolution, *i.e.* that the intergrain necks are so large that particles are no longer distinguishable. This experiment has shown that it is possible to follow the microstructure evolution during the sintering in real time. It is made possible through the development of high-resolution detection employing radiation hard optics and a fast CCD camera. The most recent development uses the 1M60 Dalsa camera and allows a frame rate of up to 60 frames s^{-1}. ID15 obtains a complete tomography data set

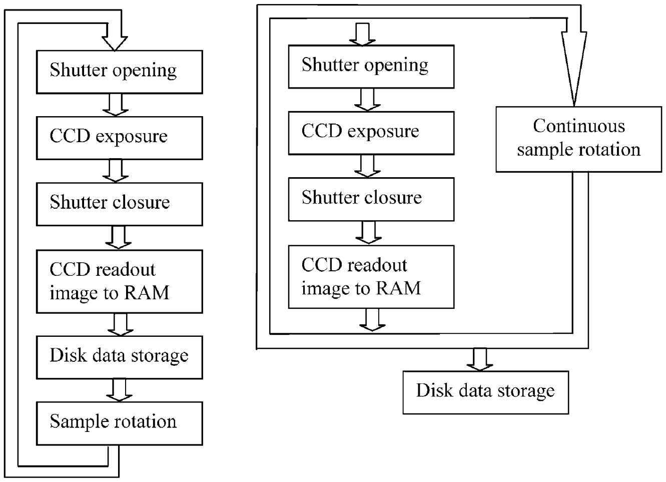

Figure 14
Left: data acquisition system for step-by-step sample rotation, typical data acquisition time 15 min. Right: data acquisition system for fast continuous rotation mode for rapid imaging (scan times down to 30 s), typical data acquisition time 30 s with Frelon camera.

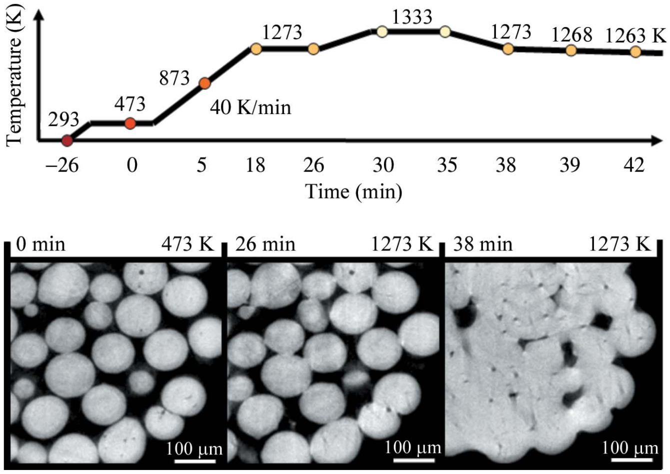

Figure 15
Thermal cycle for copper powder sample and two-dimensional projections of Cu particles at different stages of the sintering.

of 750 projections with 1024 × 1024 pixel images in 15 s, covering an angular rotation of 180°.

8. Conclusions

The spatial resolution of a detector based on a scintillator, microscope optics and a CCD camera is limited by the diffraction limit of the optics to about 0.4 µm (depending on the wavelength of the scintillation light and the numerical aperture of the microscope), but practically, scattering and undesired emission from substrate limits the resolution to 0.5 µm (Koch *et al.*, 2000). The present generation of high-resolution X-ray imaging detectors are limited in terms of efficiency owing to the high spatial resolution required which needs a very thin, and thus low X-ray absorption, screen that emits the visible light. The combination of single-crystal scintillator films with optical magnification is still under development. GGG:Eu single-crystal film has an improved performance as compared with the LAG:Eu scintillator, *i.e.* the conversion efficiency is doubled and the undoped GGG substrate does not show luminescence under X-ray excitation. More measurements will be made to quantify the afterglow and the tail of the line spread function with a GGG:Eu epitaxial layer.

There is demand for a detector equipped with up to three objectives, with motorized focusing and choice of microscope objective lens. The goal here is to use the same detector head and to change the objectives without manual intervention, *i.e.* to improve the spatial resolution or the field of view during the experiment without changing the detector.

The latest performance for the tomography sequence is 30 s for 750 projections with the Frelon camera at 14-bit dynamic range and 15 s for the Dalsa 1M60 at 12-bit dynamic range using its dedicated acquisition system. The Frelon 2k14, 2048 × 2048 pixels, can reach 15 frames s^{-1} in frame transfer mode with 1 ADU of read noise. Faster acquisition of 60 frames s^{-1} is possible with the Dalsa 1M60, 1024 × 1024 pixels, with 1 ADU of readout noise. This performance is also the result of using an efficient scintillator and a new optical design based on a reflecting objective.

An improvement in spatial resolution down to 250 nm is possible by using a scintillator at shorter wavelength (UV emission) than the present scintillator emitting in the visible band. However, very high spatial resolution requires a reduction in the thickness of the scintillator and hence a poorer efficiency of the detector system. The use of an X-ray lens, *e.g.* a Fresnel zone plate or a compound refractive lens, between the sample and the X-ray detector, as imaging device has the potential to overcome these limitations and reach 100 nm spatial resolution.

We thank C. Dujardin, C. Leluyer, J. Mugnier (LPCML, Lyon University, France) for providing the sol–gel films, M. Couchaud, B. Ferrand, A. Caillet (CEA, Grenoble, France) for growing GGG and LGG layers, and all staff of the ESRF for fast microtomography development; the members of ID15, D. Fernandez for the acquisition aspects, J. C. Labiche for the Frelon camera and J. Borrel for the mechanical design.

References

Badel, X., Galeckas, A., Linnros, J., Kleimann, P., Fröjdh, C. & Petersson, C. S. (2002). *Nucl. Instrum. Methods A*, **487**, 129–135.

Beckmann, F. (2001). *Proc. SPIE*, **4503**, 34–41.

Bravin, A., Fielder, S., Coan, P., Labiche, J.-C., Ponchut, C., Peterzol, A. & Thomlinson, W. (2003). *Nucl. Instrum. Methods A*, **510**, 35–40.

Chen, K., Kromin, A., Ulmer, M. P., Wessels, B. W. & Backman, V. (2003). *Opt. Commun.* **228**, 1–7.

Cloetens, P. (1999). Thesis, University of Brussels, Germany.

Cloetens, P. (2004). Personal communication.

Cloetens, P., Ludwig, W., Baruchel, J., Van Dyck, D., Van Landuyt, J., Guigay, J. P. & Schlenker, M. (1999). *Appl. Phys. Lett.* **75**, 2912–2914.

De Carlo, F., Albee, P., Chu, Y. S., Mancini, D. C., Tieman, B. & Wang, S. Y. (2001). *Proc. SPIE*, **4503**, 1–13.

Dujardin, C., Le Luyer, C., Martinet, C., Garapon, C., Mugnier, J., Murrillo, A. G., Pedrini, C. & Martin, T. (2005). *Nucl. Instrum. Methods A*, **537**, 237–241.

Eijk, C. W. E. (2003). *Nucl. Instrum. Methods A*, **509**, 17–25.

Flannery, B. P., Deckman, H. W., Roberge, W. & D'Amico, K. (1987). *Science*, **237**, 1439–1444.

Garcia-Murillo, A., Le Luyer, C., Dujardin, C., Martin, T., Garapon, C., Pedrini, C. & Mugnier, J. (2002). *Nucl. Instrum. Methods A*, **486**, 181–185.

Gruner, S. M., Tate, M. W. & Eikenberry, E. F. (2002). *Rev. Sci. Instrum.* **73**, 2815–2842.

Ham, K., Jin, H., Butler, L. G. & Kurtz, R. L. (2002). *Rev. Sci. Instrum.* **73**, 1521–1523.

Hamada, M., Costa, F., Shimizu, S. & Kubota, S. (2002). *Nucl. Instrum. Methods A*, **486**, 330–335.

Hignette, O., Cloetens, P., Lee, W. K., Ludwig, W. & Rostaing, G. (2003). *J. Phys. IV Fr.* **104**, 231–234.

Hoheisel, M., Giersch, J. & Bernhardt, P. (2004). *Nucl. Instrum. Methods A*, **531**, 75–81.

Jung, H., Kim, H., Hong, S., Hong, J., Jeong, H., Ho Je, J., Kim, B. & Yoo, H. (2002). *IEEE Trans. Nucl. Sci.* **49**, 2262–2267.

Kimura, S., Matsumura, T., Kinoshita, K., Hirano, K. & Kihara, H. (1998). *J. Synchrotron Rad.* **5**, 1079–1081.

Kinoshita, K., Matsumura, T., Inagaki, Y., Hirai, N., Sugiyama, M., Kihara, H., Watanabe, N., Shimanuki, Y. & Yagashita, A. (1992). *X-ray Microscopy III*, edited by A. Michette, G. Morrison and C. Buckley, pp. 335–337. Berlin: Springer.

Koch, A., Cloetens, P., Ludwig, W., Labiche J. C. & Ferrand, B. (2000). In *Proceedings of the 5th International Conference on Inorganic Scintillators and their Applications (SCINT99)*, 16–20 August 1999, Moscow State University, Moscow, Russia.

Koch, A., Perrin, F., Heurtier, P., Ferrand, B., Chambaz, B., Ludwig, W. & Couchaud, M. (1999). *Proc. SPIE*, **3659**, 170–179.

Koch, A., Raven, C., Spanne, P. & Snigirev, A. (1998). *J. Opt. Soc. Am. A*, **15**, 1940–1951.

Lame, O., Bellet, D., Di Michiel, M. & Bouvard, D. (2003). *Nucl. Instrum. Methods B*, **200**, 287–294.

Lee, H. R., Lai, B., Yun, W., Mancini, D. C. & Cai, Z. (1997). *Proc. SPIE*, **3149**, 257–264.

Lengeler, B., Schroer, C. G., Richwin, M., Tümmler, J., Drakopoulos, M., Snigirev, A. & Snigireva, I. (1999). *Appl. Phys. Lett.* **74**, 3924–3926.

Lennstrom, K., Limmer, S. J. & Cao, G. (2003). *Thin Solid Films*, **434**, 55–61.

Livet, F., Bley, F., Mainville, J., Caudron, R., Mochrie, S. G. J., Geissler, E., Dolino, G., Abernathy, D., Grübel, G. & Sutton, M. (2000). *Nucl. Instrum. Methods A*, **451**, 596–609.

Nagarkar, V. V., Miller, S. R., Tipnis, S. V., Gaysinskiy, V., Lempicki, A. & Brecher, C. (2001). *Proc. SPIE*, **4503**, 265–273.

Nagarkar, V. V., Tipnis, S. V., Gupta, T. K., Miller, S. R., Gaysinskiy, V. B., Klugerman, Y., Squillante, M. R., Entine, G. & Moses, W. W. (1999). *IEEE Trans. Nucl. Sci.* **46**, 232–236.

Nöhammer, B., Hoszowska, J., Herzig, H. P. & David, C. (2003). *J. Phys. IV Fr.* **104**, 193–196.

Robertson, J. M. & van Tol, M. W. (1984). *Thin Solid Films*, **114**, 221–240.

Schroer, C. G., Kuhlmann, M., Hunger, U. T., Günzler, T. F., Kurapova, O., Feste, S., Frehse, F., Lengeler, B., Drakopoulos, M., Somogyi, A., Simionovici, A. S., Snigirev, A., Snigireva, I., Schug, C. & Schröder, W. H. (2003). *Appl. Phys. Lett.* **82**, 1485–1487.

Stampanoni, M., Borchert, G., Abela, R. & Rüegsegger, P. (2002). *J. Appl. Phys.* **92**, 7630–7635.

Stampanoni, M., Borchert, G., Wyss, P., Abela, R., Patterson, B., Hunt, S., Vermeulen, D. & Rüegsegger, P. (2002). *Nucl. Instrum. Methods A*, **491**, 291–301.

Tate, M. W., Gruner, S. M. & Eikenberry, E. F. (1997). *Rev. Sci. Instrum.* **68**, 47–54.

Tseng, P., Hwang, C. S. & Bong, Y. F. (2000). *SRRC Annual Report*, pp. 163. SRRC, Novosibirsk, Russia.

Uesugi, K., Suzuki, Y., Yagi, N., Tsuchiyama, A. & Nakano T. (2001). *Proc. SPIE*, **4503**, 291–298.

Wang, Y., De Carlo, F., Mancini, D. C., McNulty, I., Tieman, B., Bresnahan, J., Foster, I., Insley, J., Lane, P., Laszewski, G., Kesselman, C., Su, M. & Thiebaux, M. (2001). *Rev. Sci. Instrum.* **72**, 2062–2068.

Woody, C. L., Kierstead, J. A., Levy, P. W. & Stoll, S. (1992). *IEEE Trans. Nucl. Sci.* **39**, 524–531.

Yagi, N., Inoue, K. & Oka, T. (2004). *J. Synchrotron Rad.* **11**, 456–461.

Zorenko, Y., Konstankevych, I., Globus, M., Grinyov, B. & Lyubinskiy, V. (2003). *Nucl. Instrum. Methods A*, **505**, 93–96.